Intersubband transitions in a p-type δ-doped SiGe/Si quantum well

S. K. Chun, D. S. Pan, and K. L. Wang
Department of Electrical Engineering, Device Research Laboratory, 66-147 Engineering IV, University of California, Los Angeles, California 90024
(Received 14 December 1992)

The absorption spectrum in a p-type $Si/Si_{0.6}Ge_{0.4}/Si$ structure with a δ-doped quantum well grown on the Si(001) substrate is calculated. For the bound-to-bound intersubband transitions, the depolarization effect due to the complicated couplings among valence bands is included and the inclusion of this effect is found to be essential in understanding the absorption spectrum. The effects of subband multiplicity, nonparabolicity, and valence-band anisotropy are also incorporated into an implicit formula for an effective plasma frequency in order to facilitate the calculation. For the bound-to-continuum intersubband transition, the large-box model is adopted to circumvent the difficulty in normalizing the traveling wave function of the continuum state. The depolarization effect is not significant for the latter bound-to-contiuum transition because of the small overlap of the initial- and final-state wave functions. In this case, the absorption for the normal-incidence light becomes larger than that for the parallel-incidence light. The total absorption including the bound-to-bound and bound-to-continuum intersubband transitions shows a good agreement with the experimental data. The results provide a better understanding of intersubband transition in the valence band and further show that normal-incidence transitions can be significant.

I. INTRODUCTION

Intersubband transitions in quantum wells have attracted a great deal of interest due to the potential applications in modulators and infrared (IR) detectors.[1,2] The intersubband transition energy in the quantum well is easily tunable by varying the quantum-well width and barrier height. Moreover, there is a potential for the fabrication of uniform IR detector arrays with large area. West and Eglash[1] reported the intersubband transitions using an n-type $GaAs/Al_xGa_{1-x}As$ quantum-well structure, and thereafter much progress has been made in making IR detectors and arrays.[3–5] For the n-type $GaAs/Al_xGa_{1-x}As$ quantum-well structure, only the optical field parallel to the quantum-well growth direction (designated the z polarization) causes the intersubband transition.[1,2] This is due to the fact that electron motion in the quantum-well direction (the z direction) is necessary for the intersubband transition of a spherically symmetric valley. Such motion can only be induced by the optical field along the quantum-well direction. For an n-type SiGe/SiGe quantum-well structure, however, the polarization selection rule stated above can be changed due to the anisotropic mass tensor of the ellipsoidal valleys. The optical field polarized normal to the quantum-well growth direction (the x polarization) can induce intersubband transitions depending on the growth direction.[6,7] Also, the oscillator strength for the intersubband has been shown to depend on the growth direction and the strain condition.[8]

Recently, p-type quantum wells have also been demonstrated to have possible applications for IR detectors. A detailed calculation of the transitions among the valence bands for p-type $GaAs/Al_xGa_{1-x}As$ quantum wells indicates that both x- and z-polarized fields can induce the absorption due to the couplings between the s-type conduction band and p-type valence bands (s-p coupling).[9] This result suggests a normal incidence application for the IR detector, the modulator, and other optical devices.

More recently, the intersubband transitions in p-type SiGe/Si heterostructures with a δ-doped quantum well have been experimentally demonstrated by Park, Karunasiri, and Wang.[10] In that paper, the observed transition peak in the 6-μm range was explained to be the confined-to-confined transition between two heavy-hole subbands. Another peak in the 3-μm range was attributed to the bound-to-continuum transition. The experimental data for the bound-to-bound transition cannot be understood from the model of Chang and James,[9] who used a two-band model to treat the p-type $Al_xGa_{1-x}As/GaAs$ quantum well for the bound-to-bound transition. First of all, with the framework of Chang and James,[9] one cannot explain the unusually large width of the peak observed by Park, Karunasiri, and Wang. Moreover, there is only one peak, and transitions among various different valence bands appear absent.

For the bound-to-continuum intersubband transition observed in the work of Park, Karunasiri, and Wang, the absorption for the x-polarized field is the strongest. The Bloch function of the ground heavy-hole band is only a function of the plane directions, and thus the largest absorption occurs for the polarized field along the plane[10] (normal incidence). This fact is true for the first-order approximation. However, since the valence bands are strongly coupled among them as well as with the conduction band, the depolarization dependence becomes more complicated. Previously, Allen, Tsui, and Vinter[11] and Ando[12] formulated the effect of depolarization in intersubband absorption for the n-type inversion layer. In

those cases, only the conduction band was involved and band multiplicity, nonparabolicity, and anisotropy were not considered. Furthermore, in the case of heavy doping, high Fermi level (occupying the high plane-wave vector) increases the couplings, and thus complicates the selection rule. Thus a refined framework for the calculation of the intersubband transition is needed.

The purpose of this work is to provide a framework to help understand the polarization dependence of intersubband transitions in the heavily doped $Si_{1-x}Ge_x/Si$ quantum-well structure. In this framework, we have generalized the treatise of the depolarization effect used in the n-type Si inversion layer[11] (for multiple subbands of the conduction band) and expanded to include the p-type case including nonparabolicity, anisotropy, and multiple-band coupling. The bound-to-continuum intersubband transition is then calculated using a large-box model and, in this case, the depolarization effect is not included due to the small overlap of the wave functions for the bound and the continuum states. Because of the coupling, the subbands are no longer the pure heavy-hole (HH), light-hole (LH), or spin-orbit (SO) states away from the zone center. Thus the transitions among subbands occur in a mixed way, involving both the same type and different types of Bloch states, and the definition "intersubband transition" is used here loosely to describe the transition among subbands, pure or mixed. The calculated results cover a wide range of the absorption spectrum involving bound-to-bound and bound-to-continuum intersubband transitions. The calculated results are compared with the published experimental results and show a good agreement.

II. INTERSUBBAND TRANSITION

A. Quantum-well structure

In the calculation, the band structure is described using a six-band $\mathbf{k}\cdot\mathbf{p}$ method formulated by six basis functions, represented by the $|J,m_J\rangle$ notation in the framework of single-particle theory. The s-type conduction band is taken into account perturbatively (all other bands have been included in an approximate way with the use of the empirical mass value). We choose the quantum-well direction (the z axis) as the quantization axis of the angular momentum.

The total 6×6 Hamiltonian includes both the $\mathbf{k}\cdot\mathbf{p}$ Hamiltonian[13,14] and the strain Hamiltonian.[15] The strain and spin-orbit coupling terms do not lift the spin degeneracy, and thus the total 6×6 Hamiltonian matrix can be factorized into two 3×3 matrices using a unitary transformation as follows:[16]

$$H=\begin{bmatrix} Z_1 & (X+j2Y)/2\sqrt{3} & -(Y+jX)/\sqrt{6} \\ & Z_2 & -[3Y\cos(\chi-2\eta)+jZ_4]/3\sqrt{2} \\ & & Z_3 \end{bmatrix}, \tag{1}$$

where the elements in the lower triangle are the complex conjugates of those in the upper triangle, and the elements of the Hamiltonian matrix are

$$\begin{aligned} Z_1&=(A+\tfrac{1}{2}B)(k_x^2+k_y^2)+(A-B)k_z^2+\epsilon_0 , \\ Z_2&=(A-\tfrac{1}{2}B)(k_x^2+k_y^2)+(A+B)k_z^2-\epsilon_0 , \\ Z_3&=A(k_x^2+k_y^2+k_z^2)-\Delta , \\ Z_4&=3B(k_x^2+k_y^2-2k_z^2)+6\epsilon_0 , \\ Xe^{j\chi}&=3B(k_x^2-k_y^2)+j2Nk_xk_y , \\ Y&=Y'k_z,\ Y'e^{j\eta}=N(k_x-jk_y) , \\ \epsilon_0&=\tfrac{2}{3}D_u(e_{zz}-e_{xx}) . \end{aligned} \tag{2}$$

The coefficients A, B, and N are the inverse mass band parameters (IMBP), and Δ is the spin-orbit splitting energy. D_u is the valence-band uniaxial deformation potential for (001),[17] and e_{ij} is the conventional strain component. The IMBP's of SiGe alloys are obtained by Lawaetz's method,[18] and D_u of the SiGe alloy is linearly interpolated assuming strain independence.[19,20] The parameters used in our calculation are listed in Table I.

First we calculate for the quantum-well structure of $Si/Si_{0.6}Ge_{0.4}/Si$ grown on Si(001) used by Park, Karunasiri, and Wang[10] for their experiment. The well width is taken to be 40 Å, in which the center 30 Å of the well are δ doped, with a doping level of 5×10^{19} cm^{-3}. The potential discontinuity is obtained using the band-offset calculations of Van de Walle and Martin[21] and People.[17] As shown in Fig. 1, the valence-band top of the strained well is taken as the zero energy level. In the calculation, we add 20-meV band bending for all valence bands due to the high doping concentration used.[22] The band bending in the well is assumed to be constant, which greatly simplifies the calculation. But this assumption causes some discrepancy in the subband separation (13–17 meV) in comparison with that obtained by the self-consistent calculation, in which the isotropic, parabolic, and decoupled valence bands were used.[10] As will be shown later, this discrepancy is also present in our case. The labels of the quantized subbands are adopted from the characteristics of the basis states at the zone center. That is, the HH1 represents the first heavy-hole-

TABLE I. Material parameters used in this work.

Parameter	Si	$Si_{0.6}Ge_{0.4}$	Ge	Unit
A	−4.22 (Ref. 18)	−5.43	−13.30 (Ref. 18)	a.u.
B	−0.79 (Ref. 18)	−1.47	−8.50 (Ref. 18)	a.u.
N	−8.61 (Ref. 18)	−11.47	−34.14 (Ref. 18)	a.u.
D_u	3.41 (Ref. 31)	3.37	3.32 (Ref. 32)	eV

type subband, although, strictly speaking, no rigid assignment can be made due to band mixing, as discussed previously.

In calculating the subband structure of the SiGe/Si quantum-well system, the envelope-function approximation is used, in which the wave function in each layer is written as the product of a slowly varying envelope function and the basis function of the particular semiconductor. Due to the material similarity, each SiGe layer is assumed to be represented by the same basis functions. In quantum wells, although the potential discontinuity breaks translational symmetry along the growth direction, the wave vectors in the plane directions are still good quantum numbers. Thus for a given energy E and a plane-wave vector, $\mathbf{k}_t(k_x,k_y)$, the total envelope function for each layer can be written as[23]

$$\tilde{F}(r)=[a_1\tilde{F}_h(k_{zh})e^{jk_{zh}z}+a_2\tilde{F}_l(k_{zl})e^{jk_{zl}z}+a_3\tilde{F}_s(k_{zs})e^{jk_{zs}z}+a_4\tilde{F}_h(-k_{zh})e^{-jk_{zh}z}+a_5\tilde{F}_l(-k_{zl})e^{-jk_{zl}z}+a_6\tilde{F}_s(-k_{zs})e^{-jk_{zs}z}]e^{j(k_x x+k_y y)} . \quad (3)$$

where $\tilde{F}$ and $\tilde{F}_i$ are the 3×1 tensor, and $\tilde{F}_i$ is the envelope function obtained from the Gauss elimination.[23] k_{zi} is the wave vector in the growth direction obtained from the sixth-order secular equation for a given E and $\mathbf{k}_t$. From the boundary conditions[24] of the envelope function continuity and the current conservation at the interfaces, we obtain 12 linear equations for the barrier and well. The 12 linear equations are used to determine the 12 unknown coefficients needed for two barriers and one well side. For the case of the bound-to-bound transition, only decaying functions in the barrier are used, and these six coefficients are eliminated from the total of 18. For the bound-to-continuum transition, a large-box model is used in the barrier regions to eliminate six coefficients. We can set up a 12×12 determinant, and the confined energy levels are obtained from the zeros of the 12×12 determinant.

Ekenberg, Batty, and O'Relli[25] calculated the valence-subband dispersion of the strained $Si_{0.5}Ge_{0.5}$/Si quantum well using a modified variational method. We tried to reproduce the valence-subband dispersion of their structure using the method described in the preceding paragraph, and the results are in good agreement with their calculation. This demonstrates the reliability of our calculation.

Using the quantum well structure of Park, Karunasiri, and Wang,[10] we obtained the valence-subband dispersion for three different directions of the plane-wave vector: the [100] (solid line), 22.5° from [100] (dashed line), and [110] (dotted line) directions as shown in Fig. 2. The five confined subbands are also shown. The curvatures of the highest subband HH1 are very close to those of the bulk heavy-hole band for a small $\mathbf{k}_t$, and become nonparabolic as $\mathbf{k}_t$ increases. However, the other subbands show a severe nonparabolic behavior, dependent on the plane direction. This fact indicates that the valence bands are strongly mixed in the quantum well. The broadness of the intersubband transition peaks is partially due to the nonparabolic behavior of the valence subbands. Moreover, the different nonparabolic behavior of the subband energy levels depends on the direction of the plane-wave vector, and thus affects the position and magnitude of the

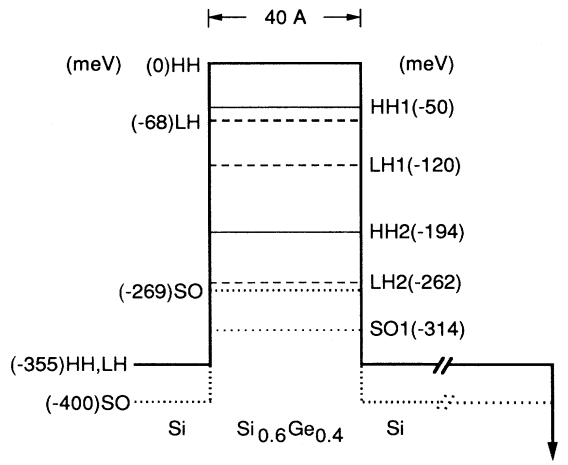

FIG. 1. The band structure of the strained $Si_{0.6}Ge_{0.4}$ quantum well grown on Si(001) with a well width of 40 Å, where the center 30 Å is doped to 5×10^{-19} cm^{-3} used in the work of Park, Karunasiri, and Wang (Ref. 10).

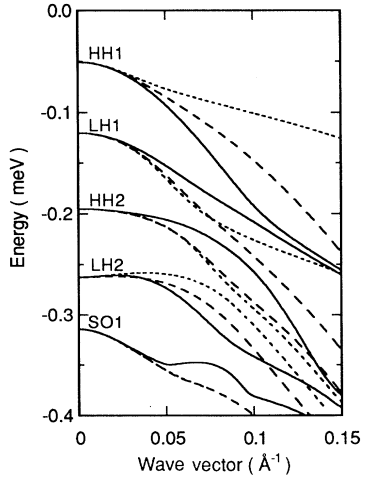

FIG. 2. The dispersion relation for the quantum well described in Fig. 1. The solid, dashed, and dotted curves are the dispersion relations for the plane-wave vector in the [100], 22.5° from the [100], and [110] directions, respectively.

absorption peak for the transition away from the zone center.

B. Bound-to-bound intersubband transition

Generally, the intersubband transition for quantum wells with a doping concentration lower than 1×10^{18} cm^{-3} is treated elsewhere. In this case, where the many-body effect may not be important, the absorption occurs at the photon energy equal to the subband separation. However, for a high carrier concentration, the absorption peak does not agree with the subband separation, as shown in the n-type inversion layer of Allen, Tsui, and Vinter[11] and Ando.[12] In those prior works, the discrepancies in the absorption energy and subband separation were explained as the result of many-body effects, depolarization, excitonlike and exchange effects.[26,27,11,12] For doping concentrations higher than 1×10^{19} cm^{-3}, the depolarization effect is expected to be dominant in shifting the absorption (resonance) frequency.[22] For a two-level system, the resonance frequency ω_r is shifted to a higher frequency $\omega_{r'}$, due to plasma effects:[11]

$$\omega_{r'}^2=\omega_r^2+\omega_p^2 , \tag{4}$$

where ω_p is the plasma frequency. However, the above rule is valid only when two subbands are employed and those subbands are assumed to be isotropic and parabolic. For a three-level system, Allen, Tsui, and Vinter formulated the absorption and showed that the coupling interaction gives rise to a change of the absorption line shape when the level broadening is included. When involving the nonparabolic and anisotropic nature of the multiple valence subbands, as in our case, the coupling interactions among the oscillators become essential (each transition being considered as an oscillator).

To include the depolarization effect in the calculation of the intersubband absorption for the valence band, we follow the scheme of Allen, Tsui, and Vinter. However, that nonparabolicity and anisotropy were not included in their formulation. We have included these effects in our formulation. In doing this, the integral for the depolarization charge, $\Delta n_m(z)$, becomes

$$\Delta n_m(z)=-2\sum_{n,\mathbf{k}_t}\frac{e}{\hbar}\frac{\omega_{nm}(\mathbf{k}_t)}{\omega_{nm}^2(\mathbf{k}_t)-\omega^2+j\omega/\tau_{nm}}\times\psi_n^*(z,\mathbf{k}_t)\psi_m(z,\mathbf{k}_t)\times\langle\psi_n(\mathbf{k}_t)|\phi|\psi_m(\mathbf{k}_t)\rangle , \tag{5}$$

where τ_{nm} and ω_{nm} are the lifetime and frequency for the subband separation between the initial state m and the final state n, respectively, ω is the incident photon frequency, and ω/τ_{nm} indicates a level broadening. ψ_m and ψ_n are the initial and final states, respectively, and ϕ is the perturbing potential as a result of photon absorption. The perturbing potential along the growth direction may be written from Poisson's equation as

$$\frac{\partial^2\phi}{\partial z^2}=-\frac{e}{\epsilon}\Delta n_m(z) , \tag{6}$$

where ϵ is the dielectric constant. From Eqs. (5) and (6), a set of coupled linear equations can be written as

$$-\varepsilon z_{nm}(\mathbf{k}_t)=\phi_{nm}(\mathbf{k}_t)+\sum_{n',\mathbf{k}_t'}\frac{2e^2}{\epsilon\hbar}\frac{\omega_{n'm}(\mathbf{k}_t')}{\omega_{n'm}^2(\mathbf{k}_t')-\omega^2+j\omega/\tau_{n'm}}\phi_{n'm}(\mathbf{k}_t')S(n,\mathbf{k}_t,n',\mathbf{k}_t') , \tag{7}$$

where $z_{nm}(\mathbf{k}_t)$ and $\phi_{nm}(\mathbf{k}_t)$ are the simplified forms of the dipole and perturbing potential matrix elements, respectively, for a given $\mathbf{k}_t$. $S(n,\mathbf{k}_t,n',\mathbf{k}_t')$ is a product of two overlaps of the involved wave functions as defined by Allen, Tsui, and Vinter.[11] To simplify the calculation, the square of $S(n,\mathbf{k}_t,n',\mathbf{k}_t')$ is evaluated as the product of $S(n,\mathbf{k}_t,n,\mathbf{k}_t)\times S(n',\mathbf{k}_t',n',\mathbf{k}_t')$, since the evaluation of $S(n,\mathbf{k}_t,n',\mathbf{k}_t')$ is much more time consuming (CPU). We have compared these two calculations and the results are very close. Thus for all subsequent calculations, we use the latter to evaluate $S(n,\mathbf{k}_t,n',\mathbf{k}_t')$. In doing this, we choose the single particle Bloch state without including the effect of the random distribution of the acceptors. The effect of the random charge distribution, sometimes referred to as a band-tailing effect, is included in the lifetime τ.

It should be noted that the above linear equations are $\mathbf{k}_t$ dependent, and a large set of linear equations is needed in order to account for the subband nonparabolicity and anisotropy. Thus it becomes an immense task for computation for each oscillator (between the m and n states). To circumvent this problem, instead of solving the linear equations directly, we define a $\mathbf{k}_t$-dependent plasma frequency to account for the coupling among the oscillators:

$$\omega_{pnm}^2(\mathbf{k}_t)=\sum_{n',\mathbf{k}_t'}\frac{2e^2}{\epsilon\hbar}\omega_{n'm}(\mathbf{k}_t')S(n,\mathbf{k}_t,n',\mathbf{k}_t')\times\frac{\phi_{n'm}(\mathbf{k}_t')}{\omega_{n'm}^2(\mathbf{k}_t')-\omega^2+j\omega/\tau_{n'm}}\times\frac{\omega_{nm}^2(\mathbf{k}_t)-\omega^2+j\omega/\tau_{nm}}{\phi_{nm}(\mathbf{k}_t)} . \tag{8}$$

With the complex plasma frequency defined above, the relation between the perturbing potential and optical matrix element shown in Eq. (7) can be rewritten as

$$\frac{\phi_{nm}(\mathbf{k}_t)}{\omega_{nm}^2(\mathbf{k}_t)-\omega^2+j\omega/\tau_{nm}}=\frac{-\varepsilon z_{nm}(\mathbf{k}_t)}{\omega_{nm}^2(\mathbf{k}_t)+\omega_{pnm}^2(\mathbf{k}_t)-\omega^2+j\omega/\tau_{nm}} , \tag{9}$$

where ε is the electric field produced by the carrier distribution. Equation (9) shows that the dipole matrix element z_{nm} is not linearly proportional to the perturbing potential matrix element, since these plasma frequencies are also functions of ϕ_{nm}. For an incoming photon, the oscillators respond to the perturbing potential with a shifted response frequency. Equation (9) is inserted into Eq. (8), and the complex plasma frequency can be written as

$$\omega_{pnm}^2(\mathbf{k}_t)=\sum_{n',\mathbf{k}_t'}\frac{2e^2}{\epsilon\hbar}\omega_{n'm}(\mathbf{k}_t')S(n,\mathbf{k}_t,n',\mathbf{k}_t')\frac{z_{n'm}(\mathbf{k}_t')}{z_{nm}(\mathbf{k}_t)}\frac{\omega_{nm}^2(\mathbf{k}_t)+\omega_{pnm}^2(\mathbf{k}_t)-\omega^2+j\omega/\tau_{nm}}{\omega_{n'm}^2(\mathbf{k}_t')+\omega_{pn'm}^2(\mathbf{k}_t')-\omega^2+j\omega/\tau_{n'm}} . \tag{10}$$

As seen in Eq. (10), the above plasma frequency for the n and m states at $\mathbf{k}_t$ is affected by other plasma frequencies due to the coupling among the oscillators. If the $\mathbf{k}_t$-dependent plasma frequencies are determined simultaneously, the coupling interactions among the oscillators can be effectively considered without solving the large set of linear equations. Instead, Eq. (10) can be easily solved by iteration, beginning the evaluation without coupling. When the broadening ($\hbar/\tau_{nm}$) caused by damping is smaller than 30 meV, the plasma frequency converges slowly near the resonance frequency for each $\mathbf{k}_t$. Fortunately, in this case, the depolarization is small and may be ignored. For broadening larger than 30 meV, as in our case, the plasma frequency converges readily and the coupling among oscillators is easily taken into account. In our calculation, we used 31 directions of the wave vector between the [100] and [010] directions, and, for each direction, the larger value of the wave vector is continuously used until the carrier occupancy of the lowest subband is negligibly small.

For a two-level system with parabolic and isotropic subbands, the above plasma frequency for all $\mathbf{k}_t$'s is reduced to a constant value, and thus the resonance frequency can be represented by Eq. (4). However, for the case of a multilevel system with nonparabolic and anisotropic subbands, the plasma frequency is $\mathbf{k}_t$ dependent and becomes a complex value depending on the level broadening as well as the transition frequency. In this case, the plasma frequency can be separated into two parts as

$$\omega_{pnm}^2(\mathbf{k}_t)=\sum_{\mathbf{k}_t'}\Omega_{pnm}^2(\mathbf{k}_t')+\sum_{n'\neq n,\mathbf{k}_t'}\Omega_{pn'm}^2(\mathbf{k}_t') . \tag{11}$$

The first term is the contribution from the same subband n with different $\mathbf{k}_t'$. Near the shifted resonance frequency ($\omega^2\sim\omega_{nm}^2+\omega_{pnm}^2$), the change of the subband separation in the same band is small compared with that of the damping term, $\hbar/\tau_{nm}$ (≥ 30 meV). In this case, the first term is mainly real. The second term is the contribution from the other subbands n'. Because of large subband separations, the second term is complex and has a large imaginary part near the shifted resonance frequency. When $\omega_{nm}(\mathbf{k}_t)>\omega_{n'm}(\mathbf{k}_t')$, the latter imaginary part is negative, as seen from Eq. (10). Whereas, for $\omega_{nm}(\mathbf{k}_t)<\omega_{n'm}(\mathbf{k}_t')$, it is positive. The change in ω_{pnm} will substantially affect the absorption spectra for the highly doped case, as will be explained later.

From the procedure of Allen, Tsui, and Vinter,[11] the absorbed power can be obtained by

$$P=\tfrac{1}{2}\mathrm{Re}\left[-j\omega\sum_{n,\mathbf{k}_t}\frac{2e^2}{\hbar}\omega_{nm}(\mathbf{k}_t)|\phi_{nm}(\mathbf{k}_t)|^2\right] . \tag{12}$$

By inserting Eq. (9) into Eq. (12), the absorbed power can be expressed in terms of the dipole matrix element and plasma frequency by the relation

$$P=\sum_{n,\mathbf{k}_t}\frac{e^2\omega_{nm}(\mathbf{k}_t)\omega^2}{\hbar\tau_{nm}}\times\left|\frac{\varepsilon z_{nm}(\mathbf{k}_t)}{\omega_{nm}^2(\mathbf{k}_t)+\omega_{pnm}^2(\mathbf{k}_t)-\omega^2+j\omega/\tau_{nm}}\right|^2 . \tag{13}$$

The depolarization effect of the above absorption power is derived from the assumption that the perturbing potential ϕ is only the function of z. In other words, we assume that only the polarized field in the growth direction can result in a perturbing potential, allowing the dipole matrix element to be expressed in terms of the optical matrix element as

$$|\varepsilon z_{nm}(\mathbf{k}_t)|^2=\left|\frac{2A_0}{m_0}\langle\psi_n(\mathbf{k}_t)|(\hat{\epsilon}\cdot\mathbf{p})_{\epsilon_z}|\psi_m(\mathbf{k}_t)\rangle\right|^2 , \tag{14}$$

where A_0 is the vector potential due to the incoming photon,[28] m_0 is a free-electron mass, and $\hat{\epsilon}$ is the unit polarization vector of the incident photon. The absorption coefficient for the bound-to-bound intersubband transition can be represented as the superposition of the responses of a collection of damped oscillators (each with different n and $\mathbf{k}_t$) plus a plasma frequency shift (in a quadratic fashion) as

$$\alpha_m'(\omega)=\sum_n\frac{e^2}{\pi^2\hbar c\epsilon_0 n_r m_0^2 L}\int d^2k_t(f_m-f_n)|\langle\psi_n(\mathbf{k}_t)|(\hat{\epsilon}\cdot\mathbf{p})_{\epsilon_z}|\psi_m(\mathbf{k}_t)\rangle|^2\frac{\omega_{nm}(\mathbf{k}_t)/\tau_{nm}}{|\omega_{nm}^2(\mathbf{k}_t)+\omega_{pnm}^2(\mathbf{k}_t)-\omega^2+j\omega/\tau_{nm}|^2}$$
$$+\sum_n\frac{e^2}{\pi^2\hbar c\epsilon_0 n_r m_0^2 L}\int d^2k_t(f_m-f_n)|\langle\psi_n(\mathbf{k}_t)|(\hat{\epsilon}\cdot\mathbf{p})_{\epsilon_x,\epsilon_y}|\psi_m(\mathbf{k}_t)\rangle|^2\frac{\omega_{nm}(\mathbf{k}_t)/\tau_{nm}}{|\omega_{nm}^2(\mathbf{k}_t)-\omega^2+j\omega/\tau_{nm}|^2} , \tag{15}$$

where L is the quantum-well width and f is the Fermi distribution function. As explained before, the first term of Eq. (11), or the plasma frequency due to the same subband at near the resonance frequency is mainly real. The real value of the plasma frequency causes the shift of the resonance peak position similar to that of Eq. (4). On the other hand, the coupling interaction from the lower subbands (smaller resonance energy) induces the large negative imaginary part [the second term of Eq. (11)]. Thus the coupling interaction due to the lower subband effectively decreases the damping constant (ω/τ_{nm}) in Eq. (15). In other words, it decreases the width and increases the absorption coefficient. Likewise, the coupling interaction with the higher subbands effectively broadens the absorption peak, since the higher subband (large resonance energy) provides a positive imaginary value.

The optical matrix element $\hat{\epsilon}\cdot\mathbf{p}$ in Eq. (15) can be obtained from the $\mathbf{k}\cdot\mathbf{p}$ matrix element. The optical matrix element has the same form as the $\mathbf{k}\cdot\mathbf{p}$ matrix element, except that $k_i k_j$ is replaced with $k_i\epsilon_j + k_j\epsilon_i$ and multiplied by a constant factor $m_0/\hbar$.[29] Then the resulting matrix is transformed by the unitary transformation which makes the 6×6 total Hamiltonian into two 3×3 Hamiltonians. The optical matrix used accounts for all directions of the polarized electric field of the incoming light. Its elements are as follows:

$$\langle u_i|\hat{\epsilon}\cdot\mathbf{p}|u_j\rangle = \frac{m_0}{\hbar}\begin{bmatrix} M_{\rm hh} & M_{\rm hl} & M_{\rm hs} \\ M_{\rm lh} & M_{\rm ll} & M_{\rm ls} \\ M_{\rm sh} & M_{\rm sl} & M_{\rm ss} \end{bmatrix}, \tag{16}$$

where the elements of the optical matrix are

$$\begin{aligned}
M_{\rm hh} &= 2(A-B)\epsilon_z k_z + (2A+B)(\epsilon_x k_x + \epsilon_y k_y)\ , \\
M_{\rm hl} &= j\frac{1}{\sqrt{3}}N(\epsilon_x\cos\eta - \epsilon_y\sin\eta)k_z - j\tfrac{1}{3}N\epsilon_z k_t\ , \\
&\quad -\sqrt{3}B(\epsilon_x k_x - \epsilon_y k_y)\cos\chi \\
&\quad +\frac{1}{\sqrt{3}}N(\epsilon_x k_y + \epsilon_y k_x)\sin\chi\ , \\
M_{\rm hs} &= \frac{1}{\sqrt{6}}N(-\epsilon_x\cos\eta + \epsilon_y\sin\eta)k_z + \tfrac{1}{6}N\epsilon_z k_t \\
&\quad +j\sqrt{6}B(\epsilon_x k_x - \epsilon_y k_y)\cos\chi \\
&\quad -\frac{2}{\sqrt{6}}N(\epsilon_x k_y + \epsilon_y k_x)\sin\chi\ , \\
M_{\rm lh} &= M_{\rm hl}^*\ , \\
M_{\rm ll} &= 2(A+B)\epsilon_z k_z + (2A-B)(\epsilon_x k_x + \epsilon_y k_y)\ , \\
M_{\rm ls} &= \left[j2\sqrt{2}B\epsilon_z + \frac{1}{\sqrt{2}}N\epsilon_x\cos(\chi-\eta) - \epsilon_y\sin(\chi-\eta)\right]k_z \\
&\quad -j\sqrt{2}B(\epsilon_x k_x + \epsilon_y k_y) \\
&\quad -\frac{1}{\sqrt{2}}N\epsilon_z k_t\cos(\chi-2\eta)\ , \\
M_{\rm sh} &= M_{\rm hs}^*\ , \\
M_{\rm sl} &= M_{\rm ls}^*\ , \\
M_{\rm ss} &= 2A\epsilon_z k_z + 2A(\epsilon_x k_x + \epsilon_y k_y)\ ,
\end{aligned} \tag{17}$$

where k_t is the magnitude of the wave vector in the plane direction.

Equation (17) shows the selection rule of the intersubband transitions for the p-type quantum well. For the intersubband transition involving the same type of basis functions ($M_{\rm hh}$ $M_{\rm ll}$, and $M_{\rm ss}$), the oscillator strength is proportional to the polarized field times the wave vector in the same direction for the isotropic band. In this case, k_z is usually larger than k_t for high confined energy levels, resulting in a large absorption for the z-polarized field. On the other hand, when the multiple bands, e.g., the heavy- and light-hole bands (or the heavy-hole and spin-orbit bands) are involved in the subband transition, three components, $\epsilon_t k_t$, $\epsilon_z k_t$, and $\epsilon_t k_z$ become pronounced. The intersubband transition due to $\epsilon_t k_t$ and $\epsilon_z k_t$ becomes large only when carriers occupy the large value of k_t (the high doping case). On the other hand, the $\epsilon_t k_z$ term is larger than the other two terms due to the large k_z.

C. Bound-to-continuum intersubband transition

In the calculation of the absorption of the bound-to-continuum transition, care must be exercised in wave-function normalization. For a single-band case, the wave functions can be normalized by assuming that the well width is negligibly narrow. However, for the multiband case, the normalization of the wave functions is not easy, and a large-box model is used in our calculation. In this method, the continuum state is assumed to be confined in a large box which is ten times wider than the SiGe well, and energy levels are calculated in a manner similar to that for the confined energy level in the quantum well. The number of subband energy levels in the large box is increased until the absorption saturates. For the bound-to-continuum transition, the depolarization effect is not included in this calculation for the following reasons. For an infinitely large box or free space, the amplitude of the wave function in the well is extremely small. Thus the overlap between the initial and final states is negligible when compared with the bound-to-bound case. For an extremely small wave-function overlap, the depolarization effect becomes negligibly small. According to the experimental data of Park, Karunasiri, and Wang,[10] the peak position is almost independent of the polarization of the incident light, supporting our previous assertion. Thus the bound-to-continuum intersubband transition can be calculated from Eq. (15) at the zero plasma frequency limit as

$$\alpha_m''(\omega) = \alpha_m'(\omega)|_{\omega_p=0}\ , \tag{18}$$

and the total absorption is the sum of the bound-to-bound and bound-to-continuum intersubband transitions, i.e., the sum of Eqs. (15) and (17).

III. RESULTS

Figures 3(a) and 3(b) show squared momentum matrix elements (SMM's) of the structure for the z- and x-polarized fields, respectively. We show the SMM's of the important intersubband transitions for the wavelength

range shorter than 10 μm. For convenience, H1L2 is defined as the transition when the initial state is HH1 and the final state is LH2. For the z polarization, as shown in Fig. 3(a), H1H2 and L1L2 are very strong for a small k_t, and decrease as k_t increases, whereas H1L2 is forbidden at the zone center and becomes large for a large k_t. This fact indicates that the heavy- and light-hole bands are strongly coupled by means of k_t. For low doping, where the carriers have a small wave vector, the absorption strength of the H1H2 is large. For high doping, the H1L2 peak is greatly enhanced because of the occupancy at high k_t. The L1L2 transition is very similar to H1H2, and the peak position is also close to the H1H2 in this case. That is, only two strong peaks, H1H2 and H1L2, are expected according to the SMM since the H1H2 and L1L2 energies overlap into one peak. For the x polarization, the SMM shown in Fig. 3(b) is smaller than that for the z polarization of Fig. 3(a). Thus it is predicted for the bound-to-bound intersubband transition that the z-polarized transition is stronger than that for the x- or y-polarized case. It is important to note that the absorption strength of the H1L2 does not vanish completely at the zone center because of the optical matrix term of $\epsilon_x k_z$. However, without the inclusion of s-p coupling, this transition (or bulklike interband transition) is extremely weak because of the orthogonality of the basis functions. The experimental proof will be shown later.

Figure 4 shows the absorption coefficient for the bound-to-bound intersubband transitions at 300 K. In this figure, the depolarization effect is not included and an infinite lifetime is assumed. Two cases are used to check the effect of the anisotropic characteristics of the valence subbands: one assumes the isotropic valence bands ($\mathbf{k}_t \| [100]$), and the other uses the anisotropic valence bands. The Fermi energy levels for the isotropic and anisotropic cases are 137 and 107 meV, respectively, for the doping density of 5×10^{19} cm^{-3}, below the top of the valence-band edge. The lower Fermi energy level for the isotropic case is due to the small density of states of the HH1 in the [100] direction. The polarization direction is chosen such that the polarized field has equal x and z components (xz polarization) or the x component only (x polarization). The conditions are equivalent to those used in the experiment by Park, Karunasiri, and Wang[10] for a polarization angle of 0° or 90° with a 45° bevel angle of the waveguide. The dotted and chain-dotted curves (designated as x-I and xz-I) are for the x- and xz-polarized fields, respectively, for the isotropic case, whereas the dashed and solid curves are for the anisotropic case (designated as x-A and xz-A). The spectrum near 9.2 μm consists of H1H2 and L1L2 as a result of nonparabolicity. As expected from SMM's in Fig. 3, these two transitions are very strong for the xz-polarized

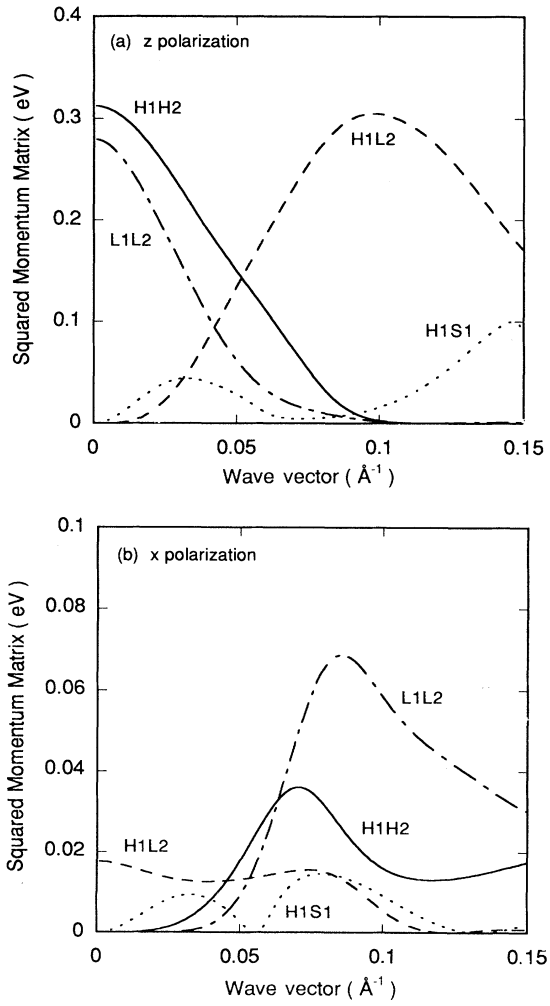

FIG. 3. Squared momentum matrix elements of the strained $Si_{0.6}Ge_{0.4}$ quantum well grown on Si(001) between various bands with a 40-Å well width. (a) z-polarized field and (b) x-polarized field.

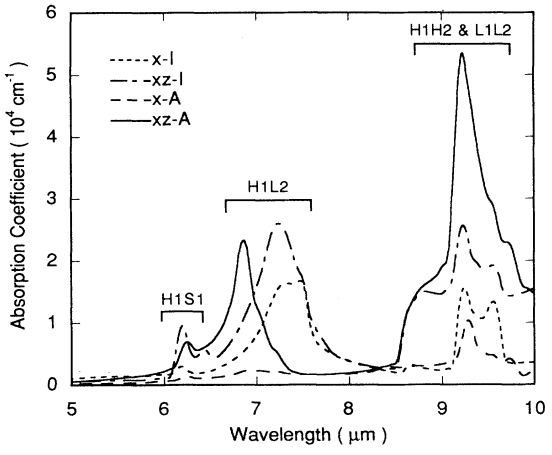

FIG. 4. The absorption coefficient of the bound-to-bound intersubband transitions without the depolarization effect. The dotted and chain-dotted curves are the absorption for the x- and xz-polarized fields, respectively, when the isotropic valence bands (x-I,xz-I) are assumed. The dashed and solid curves are for the case when the anisotropic characteristics (x-A,xz-A) are included.

field. The peak for the anisotropic case is larger than that for the isotropic case. This is mainly due to the k_t-dependent density of states and its SMM's. For the isotropic case, more carriers have larger k_t, where the SMM is small. For the x-polarized field, both cases give smaller peaks than those for the xz-polarized field, similar to the polarization dependence of the intersubband transition in the n-type quantum well. The peak near 7 μm is due to the transition from the ground heavy- to the excited light-hole subbands (H1L2), and is forbidden at the zone center. However, the band mixing among bands away from the zone center makes the transition possible, as expected from Fig. 3. The peak positions near 7 μm for the two cases are 10 meV apart, in contrast to the peak at 9.2 μm, where there is no difference in the peak positions. This fact indicates that the absorption occurs mainly away from the zone center. The transition from HH1 to SO1 gives a peak near 6.2 μm. In this case, the same parity of envelope functions and different types of Bloch states make the peak much smaller than the others.

In Fig. 4, when the peaks from the two different polarizations are compared, the anisotropic case shows that the absorption due to the xz-polarized field is much stronger than that for the x-polarized field. However, the isotropic case does not give the strong polarization dependence. That is, the isotropic case tends to overestimate the absorption for the x-polarized field. For the xz-polarized field, the H1H2 is underestimated and the H1L2 is overestimated.

As described above, the calculated absorption gives two peaks for both the isotropic and anisotropic cases. On the other hand, the experimental result of Park, Karunasiri, and Wang[10] shows only one broad peak in the region of 4~8 μm for the xz-polarized field. Several factors, which are not considered in our calculation, may account for the difference. The scattering processes, such as phonon, alloy, and impurity scatterings, may broaden the peaks to some extent. Also, the band-tailing effect due to the high doping may be important. But the inclusion of these effects alone does not make the two peaks merge into a single broad one. However, as shown next, the unusual broad peak in the experimental data can be explained by the inclusion of the depolarization effect.

Including the depolarization effect, the absorption spectra for the xz-polarized field is calculated for the bound-to-bound transition. Figure 5 shows the results for this transition along with the experimental data (given by △△△). The three calculated spectra are due to different considerations of the coupling among the subbands. The absorption from the HH1 is included only because most carriers occupy this state at 300 K. The energy broadenings $\hbar/\tau_{nm}$ for each subband are assumed to be $\mathbf{k}_t$ independent, and a constant value of 50 meV is used.[30] The dashed curve is for the isolated two-level system, neglecting the coupling interactions among subbands, but including the coupling interactions among $\mathbf{k}_t$-dependent oscillators due to the subband nonparabolicity and anisotropy. The result of assuming an isolated two-level system gives a broad peak, with the peak position near 8 μm. This peak position is 67 meV apart from the experimental peak. The chain-dotted curve shows the absorption when the coupling of the multilevel transitions plus band nonparabolicity is included, and the isotropic valence band is assumed. As mentioned earlier, the coupling of other subbands suppresses the absorption of the H1H2 transition (the lower resonance energy), while enhancing the H1L2 transition (the higher resonance energy). In this case, the peak position occurs at 6.4 μm, and the full width at half maximum (FWHM) is about 75 meV. The peak position is 30 meV apart from the experimental data, and the FWHM is somewhat narrower. When the valence-band anisotropy plus nonparabolicity and multiple subbands are included, the FWHM becomes 95 meV and the peak position moves to near 6.3 μm, and they are very close to the experimental data. The small difference of the peak position (17 meV) may be due to the lack of a self-consistent calculation. The self-consistent calculation done by Park, Karunasiri, and Wang[10] shows that the subband separation is 13~17 meV larger than ours. From the above results, the experimental data of the bound-to-bound intersubband transition can only be explained when the depolarization effect, subband multiplicity, and subband anisotropy are invoked.

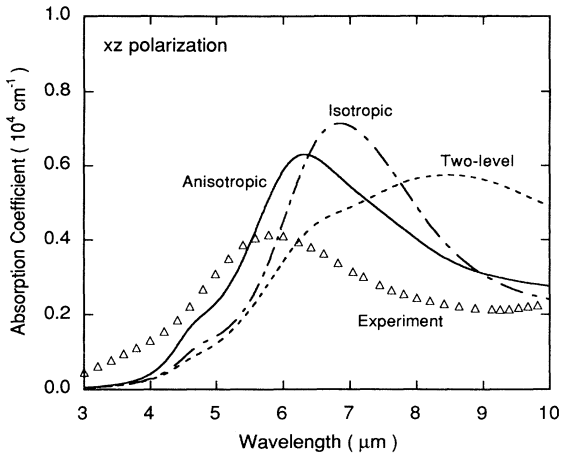

FIG. 5. The absorption coefficient of the bound-to-bound intersubband transitions, including the depolarization effect for the xz-polarized field at 300 K. The dashed curve is the absorption calculated by using an isolated two-level system and valence-band anisotropy. The chain-dotted curve is for a coupled multilevel system when the plane-wave vector in the [100] direction is used only (assuming isotropic). The solid curve is for the coupled multilevel system with the valence band anisotropy. The symbol △ denotes the experimental data (Ref. 10).

For the bound-to-continuum intersubband transition, Fig. 6 shows the measured and calculated spectra for the x polarization (normal incidence), where the absorptions from the HH1 and LH1 are included. The experimental data are given with the free-carrier contribution removed and the experimental data of the intersubband transition equal our calculation at 4.6 μm for 40% Ge and 3.6 μm for 60% Ge, respectively. The depolarization effect is not included in this case for the reason explained above. In our calculation, the direct conduction band is not explic-

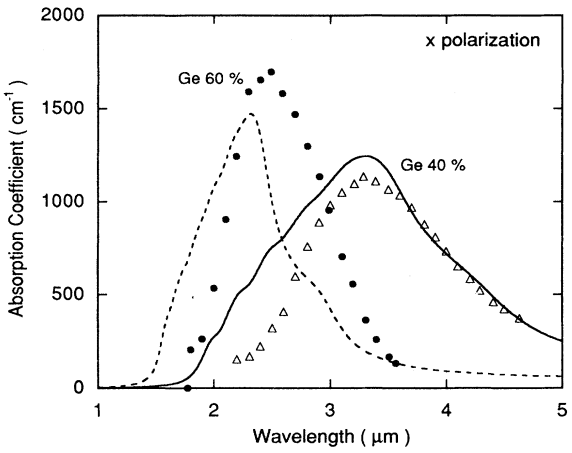

FIG. 6. The calculated absorption coefficient of the bound-to-continuum intersubband transitions for the x-polarized field at 300 K. The solid and dashed curves are the absorption for the Ge 40% and 60% quantum wells, respectively. Experimental data (Ref. 10) (shown in △ and ●) are also given for comparison.

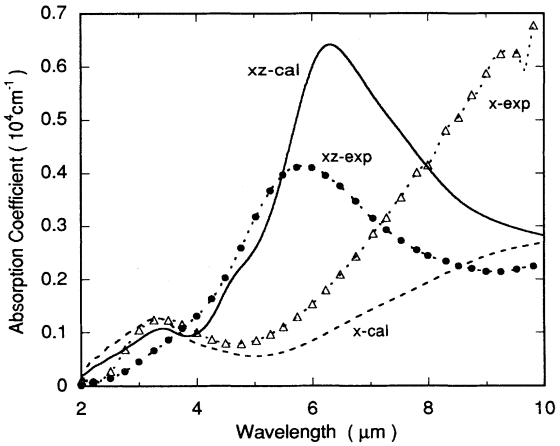

FIG. 7. The absorption coefficient for the strained $Si_{0.6}Ge_{0.4}$ quantum well grown on Si(001) with a 40-Å well width, where the center 30 Å are doped with up to 5×19 cm^{-3}. Symbols with △ and ● are experimentally obtained absorption coefficients for the x- and yz-polarized fields, respectively. The dashed and solid curves are the theoretical calculations for the corresponding fields. The experimentally obtained values include the free-carrier absorption.

itly used as a basis function. However, the s-p coupling interaction of the direct conduction band is treated as a perturbation term. Each calculated absorption spectrum has two peaks, due to two initial states: the heave-hole (HH1) and light-hole (LH1) ground states. As can be clearly seen for the 60% Ge well case, the increase in absorption strength at 2.5 μm comes from the heavy-hole ground state HH1. This contribution is larger than the other because of its larger carrier occupancy.

As the Ge content of the well increases, the peak position shifts to the lower-wavelength (higher-energy) region and its peak height increases. The lower peak position for the 60% Ge well is due mainly to the larger band offset of the quantum well. On the other hand, the change of the peak heights can be understood from the s-p coupling between the s characteristic of the direct conduction band (Γ_2') and the p-characteristic valence band (Γ_{25}'). This coupling strength is proportional to the square of the wave vector and inversely proportional to the square of the direct energy gap to the first order. Because the continuum state for the 60% Ge quantum well has the larger k_z and smaller direct energy gap, the s-p coupling for the 60% Ge quantum well becomes larger and thus gives the larger peak height.

In the data of Figs. 5 and 6, we have explained the absorption coefficient of the bound-to-bound transition for the xz polarization and the bound-to-continuum transition for the x polarization. However, the polarization dependence of the absorption has not been discussed. Figure 7 shows the polarization dependence of the calculated absorption spectra and the experimental data of 40% Ge quantum wells for the bound-to-bound and bound-to-continuum intersubband transitions. The curves with symbols are experiment data (△ for the x polarization and ● for the xz polarization), whereas the dashed and solid curves are the theoretical calculations for the x and xz polarizations, respectively. Because of the free-carrier contribution whose quantity cannot be accurately estimated, it is difficult to compare the absolute peak heights, but the trend of the polarization dependence of the calculated absorption coefficients shows a good agreement with the experimental data. For the x-polarized field (normal incidence), the peak near 3.2 μm agrees well for the calculated and experimental spectra. In this case, the discrepancy between the experiment and calculation increases as the wavelength increases. This is expected to be due to the free-carrier absorption in the experiment data. For the xz-polarized field, the calculation (solid curve) gives a small peak near 3.2 μm while no clear peak is seen in the experimental data. The reason for this discrepancy is not clear. When the peak position of the bound-to-bound transition near 6.2 μm is shifted toward the experimentally obtained peak position (5.9 μm), or when the large broadening is chosen, the small peak may be buried in the broad peak. It should be noted, however, that for the 60% Ge quantum-well case, this small peak was obtained experimentally to be in agreement with the calculation (although different in energy). In short, our calculation shows a good agreement with the experimental data.

IV. SUMMARY

The absorption spectra for the intersubband, bound-to-bound, and bound-to-continuum transitions in the p-type δ-doped quantum well were calculated with and without the depolarization effect. For the bound-to-bound intersubband transition, the energy and the width of the experimental peak can only be explained by considering the depolarization effect, including complicated effects due to the band-coupling interactions among the valence bands. For the bound-to-continuum transition, the depolarization effect seems not as important. The independence of the absorption peak position from the po-

larization angle in the experiment supports this fact. In general, the peak positions and absorption coefficients are in good agreement with the experimental data for various Ge contents of the well layer. Our calculation clearly explains the polarization dependence of the bound-to-bound and bound-to-continuum transitions in p-type SiGe quantum wells.

ACKNOWLEDGMENTS

One of the authors (S.K.C.) would like to thank Dr. R. P. G. Karunasiri for helpful discussions and supportive data. This paper was supported in part by the Air Force Office of Scientific Research and the Army Research Office.

[1]L. C. West and S. J. Eglash, Appl. Phys. Lett. **46**, 1156 (1985).
[2]B. F. Levine, K. K. Choi, C. G. Bethea, J. Walker, and R. J. Malik, Appl. Phys. Lett. **50**, 1092 (1987).
[3]B. F. Levine, R. J. Malik, J. Walker, K. K. Choi, C. G. Bethea, D. A. Kleinman, and J. M. Vandenberg, Appl. Phys. Lett. **50**, 273 (1987).
[4]B. F. Levine, C. G. Bethea, K. K. Choi, J. Walker, and R. J. Malik, J. Appl. Phys. **64**, 1591 (1988).
[5]B. F. Levine, C. G. Bethea, G. Hasnain, J. Walker, and R. J. Malik, Appl. Phys. Lett. **53**, 296 (1988).
[6]C. L. Yang and D. S. Pan, J. Appl. Phys. **64**, 1573 (1988).
[7]C. L. Yang, D. Pan, and R. Somoano, J. Appl. Phys. **65**, 3253 (1989).
[8]S. K. Chun and K. L. Wang, Phys. Rev. B **46**, 7682 (1992).
[9]Y. C. Chang and R. B. James, Phys. Rev. B **39**, 12 672 (1989).
[10]J. S. Park, R. P. G. Karunasiri, and K. L. Wang, Appl. Phys. Lett. **60**, 103 (1992).
[11]S. J. Allen, D. C. Tsui, and B. Vinter, Solid State Commun. **20**, 425 (1976).
[12]T. Ando, Z. Phys. B **26**, 263 (1977).
[13]G. Dresselhaus, A. F. Kip, and C. Kittel, Phys. Rev. **98**, 368 (1955).
[14]J. M. Luttinger, Phys. Rev. **102**, 1030 (1956).
[15]H. Hasegawa, Phys. Rev. **129**, 1029 (1963).
[16]D. A. Broido and L. J. Sham, Phys. Rev. B **31**, 888 (1985).
[17]R. People, Phys. Rev. B **32**, 1405 (1985).
[18]P. Lawaetz, Phys. Rev. B **14**, 3460 (1971).
[19]R. People, IEEE J. Quantum Electron. **QE-22**, 1696 (1986).
[20]S. K. Chun and K. L. Wang, IEEE Trans. Electron. Devices **39**, 2153 (1992).
[21]C. G. Van de Walle and R. M. Martin, Phys. Rev. B **34**, 5621 (1986).
[22]R. P. G. Karunasiri (private communication).
[23]R. Wessel and M. Altarelli, Phys. Rev. B **40**, 12 457 (1989).
[24]M. Altarelli, Phys. Rev. B **28** 842 (1983).
[25]U. Ekenberg, W. Batty, and E. P. O'Relli, J. Phys. (Paris) **48**, 553 (1987).
[26]B. Vinter, Phys. Rev. Lett. **35**, 598 (1975).
[27]T. Ando, Phys. Rev. B **13**, 3468 (1976).
[28]B. K. Ridley, *Quantum Processes in Semiconductors* (Oxford University Press, London, 1982).
[29]E. O. Kane, J. Phys. Chem. Solids **1**, 82 (1956).
[30]From the experimental data, the $\hbar/\tau$ is expected to be 50–100 meV. Here even the lowest value of the energy broadening is used, and the observed peak in the experiment is well explained.
[31]I. Balslev and P. Lawaetz, Phys. Lett. A **19**, 6 (1965).
[32]J. C. Hensel and K. Suzuki, Phys. Rev. B **9**, 4219 (1974).